processes

MDPI

Article

High-Density Seismic Signal Processing Methods for the Gongshanmiao 3D Oil Survey of the Lianggaoshan Formation in the Sichuan Basin: A Case Study

Ming Zeng [1], Bing He [2], Qingsong Tang [3], Fei Li [2], Deming Zhang [4,*], Zhigang Liu [5], Haotian Peng [2], Cong Tang [3], Xiaowei Yan [5] and Zhihui Tu [1]

[1] Exploration and Development Research Institute, PetroChina Southwest Oil and Gas Field Company, Chengdu 610041, China; zeng_ming@petro.com.cn (M.Z.); tuzhihui@petrochina.com.cn (Z.T.)
[2] Development Management Department, PetroChina Southwest Oil and Gas Field Company, Chengdu 610081, China; hbing1@petrochina.com.cn (B.H.); lifei007@petrochina.com.cn (F.L.); penghaotian@petrochina.com.cn (H.P.)
[3] Crude Oil Department, PetroChina Southwest Oil and Gas Field Company, Chengdu 610081, China; tangqingsong2008@petrochina.com.cn (Q.T.); tangcong@petrochina.com.cn (C.T.)
[4] College of Energy, Chengdu University of Technology, Chengdu 610059, China
[5] Southwest Geophysical Research Institute, BGP Inc., China National Petroleum Corporation, Chengdu 610200, China; liuzhigang01@cnpc.com.cn (Z.L.); yanxw90@163.com (X.Y.)
* Correspondence: deming_zhang0724@163.com; Tel.: +86-19136295619

Abstract

The Lianggaoshan Formation in the Gongshanmiao block of the Sichuan Basin is characterized by narrow channel sand bodies and thin layers, resulting in weak seismic responses, which leads to poor identification of small-scale fault–fracture systems. Initial high-density 3D seismic data exhibit strong shallow surface waves and significant shot-to-shot variations in energy and frequency, necessitating amplitude-preserving noise attenuation and broadband wavelet consistency processing. First, pre-stack multi-domain amplitude-preserving noise attenuation is applied, integrating surface-wave forward modeling, stationary wavelet transform, and matrix singular value decomposition to suppress complex noise. Next, robust deconvolution constrained by a target wavelet improves broadband consistency. Subsequently, anisotropic depth-domain velocity modeling and imaging under rugged topography are conducted using a well-constrained TTI initial velocity model and full-azimuth angle-domain grid tomography. Compared with conventional data, the processed high-density data significantly enhance bandwidth, structural imaging, and thin-layer resolution. Imaging continuity of small faults (6–10 m throw) is markedly improved, and the channel characterization accuracy of the Liang-2 Member increases from 180 m to 60 m. This workflow delivers high-SNR, high-resolution, and high-fidelity results, providing a reliable basis for thin-sandbody prediction and reservoir evaluation.

Keywords: Gongshanmiao; high-density data; thin sandbody; small-scale fault-fracture; prestack multi-domain denoising; desired wavelet constraint

Check for updates

Academic Editor: Qingbang Meng

Received: 29 July 2026
Revised: 1 September 2026
Accepted: 2 September 2026
Published: 15 September 2026

Copyright: © 2026 by the authors. Licensee MDPI, Basel, Switzerland. This article is an open access article distributed under the terms and conditions of the Creative Commons Attribution (CC BY) license.

1. Introduction

To support the medium- and long-term crude oil production enhancement plan of the Southwest Oilfield Company and increase production and achieve reactivation targets in the central Sichuan Basin, a pilot high-density 3D seismic project with a full-fold coverage area of 200.68 km^2 was deployed in the Gongshanmiao area. This project focuses on the

development of Jurassic tight oil and shale oil in the western Gongshanmiao block of the central Sichuan Basin. In this area, the Jurassic reservoir depositional systems are complex, characterized by rapid lateral and vertical variations in sand body distribution and strong reservoir heterogeneity [1,2]. Specifically, sand bodies in Member 1 of the Shaximiao Formation (Sha-1) exhibit complex vertical lithologic assemblages and multi-stage stacked channels. The sand bodies in the Lianggaoshan Formation are relatively thin: beach-bar sands in the Liang-2 Member typically range from 2 to 8 m in thickness, while channel sands in the Liang-3 Member range from 2 to 12.5 m, based on statistical analysis of borehole data from the study area. The Shaximiao Formation is dominated by fluvial deposits [3,4], where frequent lateral channel migration results in pronounced spatial variability in reservoir quality. Significant differences in reservoir physical properties exist both among different channels within the same sand group and within different segments of a single channel. Coupled with complex stacking patterns and sand body architecture, this extreme spatial heterogeneity poses major challenges for fine-scale reservoir prediction. In particular, individual reservoir layers in the Lianggaoshan Formation are thin, typically 1–10 m, with interbedded sandstones and mudstones, leading to weak seismic responses, high ambiguity, and substantial difficulty in thin-reservoir prediction [5,6].

The source-connecting faults and fracture systems in the Gongshanmiao area are key controllers of the formation of high-quality sweet spots in supra-source sandstones [7,8]. To accurately evaluate fault-mediated source–reservoir connectivity and delineate favorable areas using detailed sand body characteristics and reservoir prediction results, it is essential to precisely map the spatial distribution of fault and fracture zones with vertical throws exceeding 6 m. Previous studies have successfully identified major Jurassic faults with throws greater than 20 m; however, fine characterization of small-scale fault–fracture systems remains challenging due to their weak seismic responses, small scale, and poor continuity. Therefore, based on refined velocity modeling and high-resolution imaging, this study aims to evaluate and optimize fault–fracture identification methods to achieve accurate delineation of fault zones with throws > 6 m, providing a reliable basis for assessing source–reservoir connectivity and selecting sweet spots. Previous thin-sandbody predictions using conventional 3D seismic data indicate that for reservoirs with individual layer thicknesses less than 8 m, both post-stack and pre-stack attribute-based predictions show limited accuracy. Although AVO attributes exhibit certain geological sensitivities, their correlation with sand body distribution is relatively weak, making them insufficient for detailed characterization of small-scale high-quality reservoirs. Therefore, consistent broadband processing with preserved signal fidelity and amplitude is required [9], focusing on the fine prediction of small channel sand bodies with widths of ~50 m, thicknesses of 6 m, and porosities greater than 6%.

Analysis of the raw seismic data indicates that shallow surface waves are well developed in the survey area. Moreover, due to the relatively shallow burial depth of the target formations, the seismic data are particularly susceptible to surface waves and other noise interference. Consequently, effectively suppressing noise while preserving the amplitude, frequency, and phase characteristics of valid reflection signals represents a primary processing challenge. In addition, significant shot-to-shot variations in energy and frequency are observed across the area, accompanied by pronounced spatial differences in noise intensity. Spatial variations in the seismic wavelet are strongly influenced by surface conditions, source–receiver coupling, and acquisition inconsistencies, hindering accurate representation of true lateral variations in lithologic reservoir reflection characteristics [10]. This study aims to address the inconsistencies in frequency bandwidth, phase, and wavelet characteristics of seismic data in the study area by conducting broadband wavelet-consistent processing. This approach is intended to further improve the signal-to-noise ratio, resolution,

fidelity, and lateral consistency of the seismic data, thereby enhancing the comparability of reservoir responses across different areas. The resulting high-quality processed seismic data provide a reliable foundation for fine-scale prediction of thin sand bodies, identification of small-scale faults and fractures, and subsequent evaluation of favorable areas in the Lianggaoshan Formation.

2. Data Sources and Raw Data Analysis

The full-fold coverage area of this 3D seismic processing is 200 km^2, with a total of 61,814 shots and a data volume of 42 TB. Analysis of the newly acquired raw data was conducted from the following five aspects:

(1) Static Correction Analysis

The surface topography of the survey area is generally flat, with a thin low-velocity zone typically under 6 m thick. Although elevation statics were applied during initial processing, the first breaks on certain shot records still exhibit local distortion, indicating lateral heterogeneity in the near-surface velocity field and potential residual short-wavelength static errors. Such errors can compromise the stacking quality of deep reflection events and overall imaging continuity. Therefore, subsequent processing must incorporate refraction statics and tomographic statics to further enhance near-surface correction precision and mitigate the impact of residual statics on primary reflection signals.

(2) Noise Characteristics Analysis

The noise types in raw shot records are complex, mainly consisting of high-energy 50-Hz powerline noise, low-frequency surface waves, linear noise, and random noise. Among these, surface waves are well-developed, with apparent velocities generally below 2200 m/s and dominant frequencies concentrated between 5 and 20 Hz. This strong, low-frequency interference severely suppresses primary shallow reflection signals within near offsets, degrading both the recognizability and signal-to-noise ratio (SNR) of reflections in target intervals. Consequently, targeted domain filtering, surface-wave attenuation, and amplitude-preserving noise suppression techniques are required during preprocessing to effectively eliminate strong interference while preserving the amplitude, frequency, and phase characteristics of primary reflections.

(3) Frequency and Signal Characteristics Analysis

Overall, the quality of shot records is high, with clearly discernible reflection wave groups in shallow target zones, although localized shot gathers remain heavily contaminated by surface waves. Spectral analysis reveals that target formations featuring interbedded sandstones and mudstones possess a relatively broad effective frequency band (8–70 Hz), whereas mudstone-dominated formations exhibit a narrower effective frequency band (8–60 Hz). This discrepancy is likely attributable to variations in seismic attenuation, acoustic impedance contrasts, and reflection interface development under different lithological associations. In subsequent inversion and interpretation, the influence of lithological combinations on frequency responses must be thoroughly accounted for, avoiding reservoir identification based solely on amplitude or frequency attributes.

(4) Consistency Analysis

Due to surface condition variations, source/receiver disparities, and near-surface heterogeneity, energy imbalances exist across different shot gathers and among traces within the same gather. Notably, data acquired via different geophone models, nodal acquisition systems, and conventional single-point geophones demonstrate strong overall consistency in amplitude levels and frequency characteristics, indicating that instrument type exerts a minimal impact on waveform fidelity. This finding indicates a favorable

foundation for merging datasets from diverse acquisition systems, facilitating integrated processing, broadband consistency correction, and high-precision imaging.

(5) Comparison with Legacy and Neighboring Data

A comprehensive comparison among datasets acquired across different years in the survey and adjacent areas reveals that, under identical trace spacing conditions, the overall imaging quality of the 2019 and 2025 datasets is generally comparable. Further frequency-slice scanning analysis under gain-controlled conditions demonstrates that the newly acquired 2025 shot data outperform the 2019 data in both SNR and resolution within dominant frequency bands, highlighting clear advantages in signal fidelity and high-frequency preservation. Compared with the legacy public dataset Gong-115H that was acquired in 2012, the 2025 dataset displays superior reflection event continuity and clearer wave group characteristics in target intervals, yielding a marked improvement in overall imaging quality. Frequency-slice analysis further indicates that the new data preserve richer effective high-frequency components with prominent bandwidth extension, benefiting fine sequence stratigraphy, thin-layer identification, and lithology prediction, as shown in Figure 1. These enhancements are primarily attributable to upgraded acquisition equipment, optimized survey geometries, improved source/receiver coupling, and elevated near-surface correction precision, thereby establishing a more reliable data foundation for high-precision inversion, thin-reservoir prediction, and fine fault-fracture characterization.

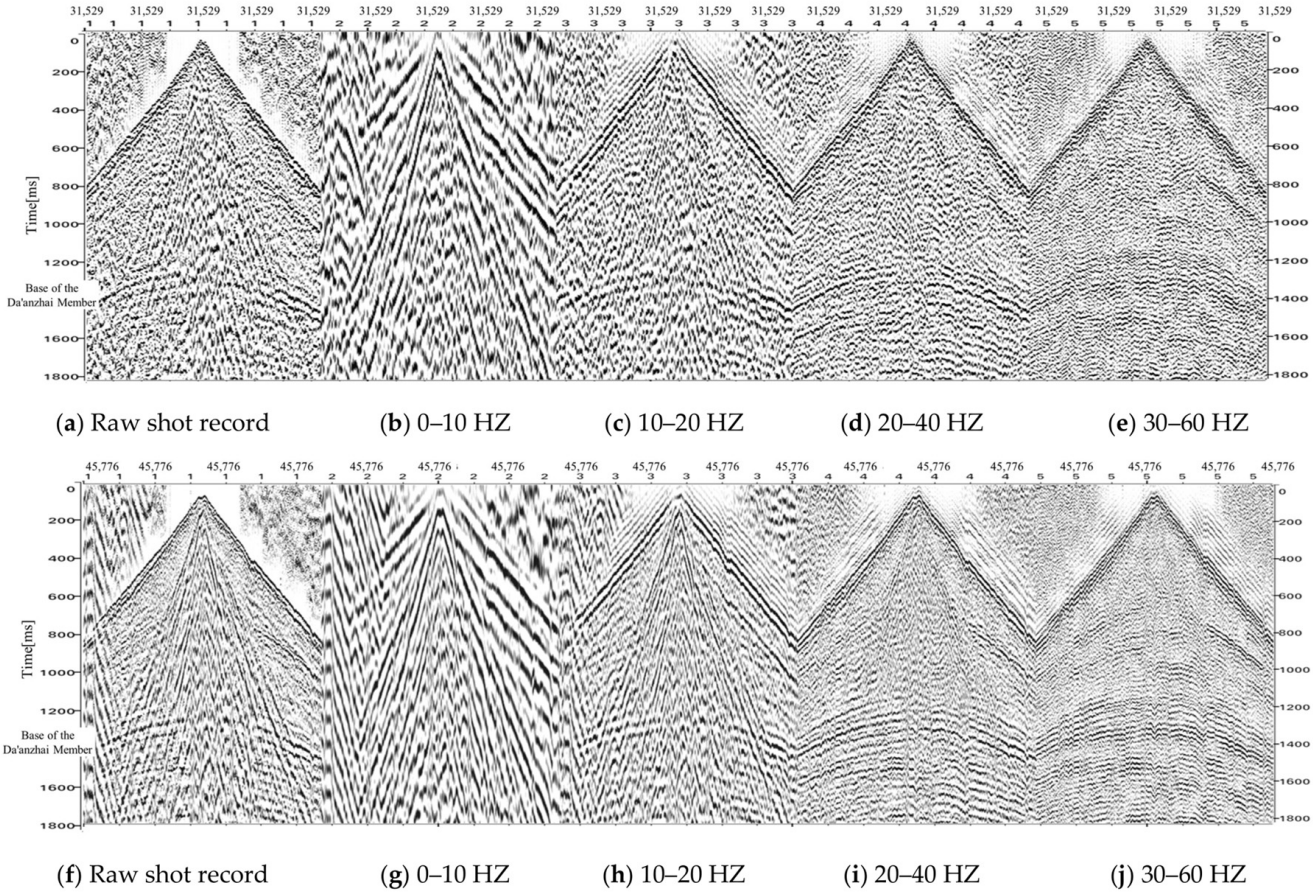


Figure 1. Frequency-dependent comparison of 3D shot gathers between the 2019 Xichong (**a**–**e**) and 2025 Gongshanmiao surveys (**f**–**j**).

3. Method

Considering the geological requirements, the core objective of this study centered on "high-fidelity, high-resolution, and high-precision imaging". Major efforts were directed toward high-fidelity noise attenuation, high-resolution processing, high-precision velocity characterization, and fine imaging workflows to significantly elevate the final data quality. This approach effectively addresses the technical demands for thin-sandbody characterization, vertical and lateral distribution delineation of high-quality reservoirs, and precise mapping of small-scale faults. The specific technical approach is illustrated in Figure 2.

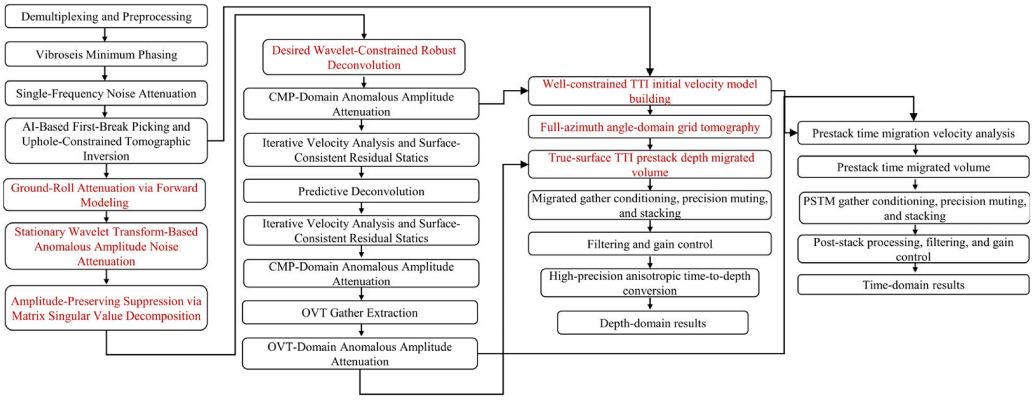


Figure 2. High-Density 3D Processing Workflow for 2025 Gongshanmiao Survey Data.

3.1. Pre-Stack Multi-Domain Amplitude-Preserving Noise Attenuation

3.1.1. Surface-Wave Attenuation via Forward Modeling

To address the lateral variations in propagation velocity and dominant frequency distribution of surface waves across the survey area [11,12], Figure 3 shows the region-customized refined suppression strategy that was adopted. Based on the dispersion characteristics of surface waves, dispersion curve forward modeling was first conducted to clarify the surface-wave modes and dispersion features across different sub-regions [13–15]. Subsequently, an adaptive surface-wave suppression algorithm was implemented to effectively separate and attenuate the noise while maximally preserving primary reflection signals, particularly low-frequency weak reflection energy. This workflow significantly enhances the fidelity of surface-wave attenuation, retaining a reliable low-frequency foundation for subsequent velocity analysis, pre-stack inversion, and deep imaging.

3.1.2. Abnormal Amplitude Noise Attenuation Based on Stationary Wavelet

To address anomalous amplitude interference in seismic data, a multi-scale suppression method based on the stationary wavelet transform (SWT) was employed [16–18]. Leveraging the shift-invariance and multi-scale decomposition capabilities of the stationary wavelet transform, this method first decomposes seismic data into different scales and frequency bands, thereby separating primary reflection signals from anomalous energy within the wavelet coefficient domain. Statistical amplitude analysis is then conducted on the wavelet coefficients at each scale to identify and locate anomalous coefficients exceeding the normal energy range. Anomalous components are attenuated via adaptive thresholding or coefficient reconstruction to effectively suppress high-amplitude burst noise [19,20].

Compared with conventional time-domain clipping or simple filtering techniques, this approach enables a finer differentiation between anomalous energy and primary reflection signals. While suppressing interference such as spikes and anomalously noisy traces, it effectively preserves the amplitude relationships, waveform characteristics, and phase information of primary signals. This significantly enhances the signal-to-noise ratio

(SNR) and data fidelity, providing a reliable data foundation for subsequent deconvolution, imaging, attribute analysis, and reservoir prediction, which is demonstrated in Figure 4.

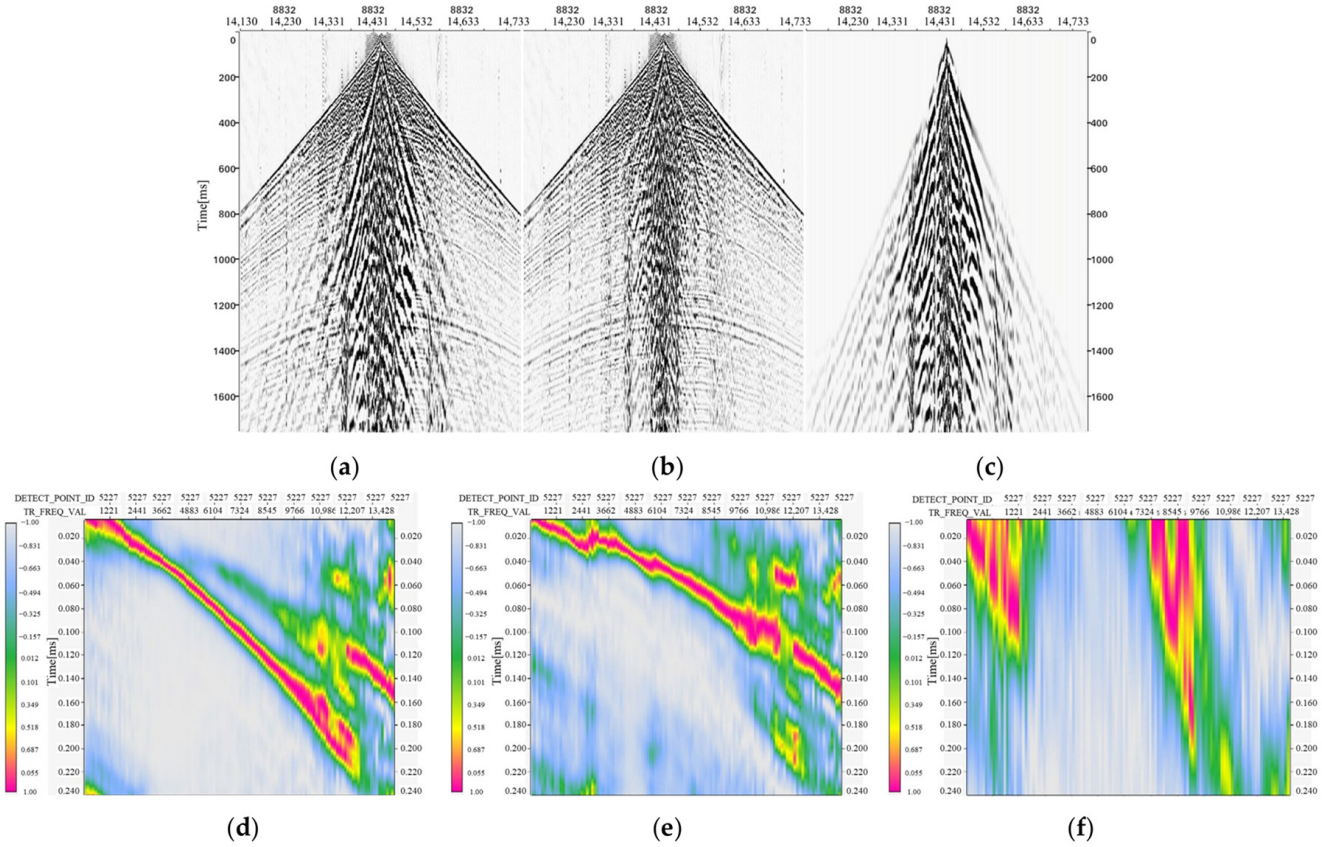


Figure 3. Comparison of results before (**a**) and after (**b**) SVD-based noise attenuation and the removed noise (**c**) and first higher-mode f-k spectrum (**d**) and second higher-mode f-k spectrum (**e**) and f-k spectrum after forward-modeling-based ground roll attenuation (**f**).

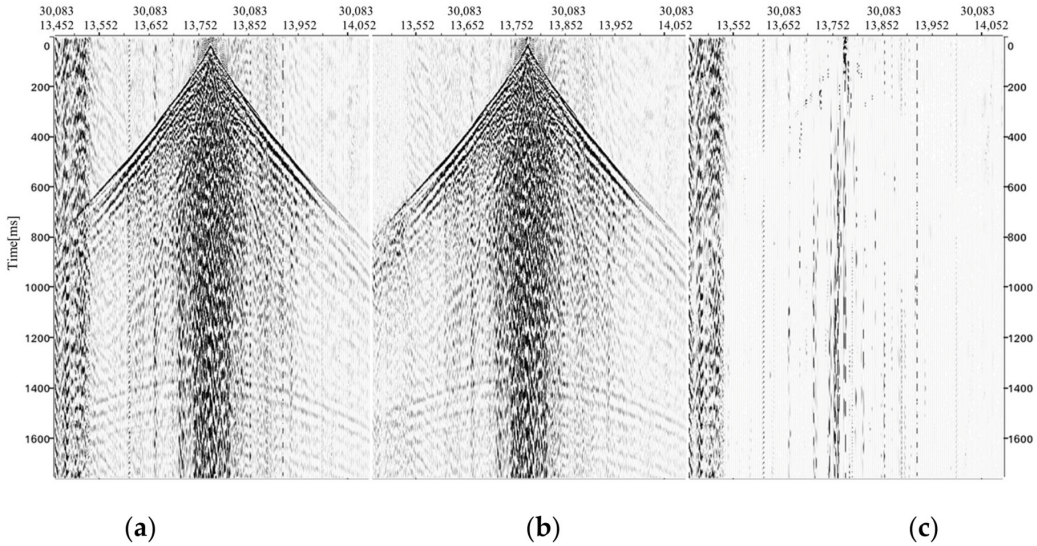


Figure 4. Comparison of seismic data before (**a**) and after (**b**) SWT-based anomalous amplitude noise attenuation and the removed noise (**c**).

3.1.3. Fidelity-Preserving Noise Suppression Based on Matrix Singular Value Decomposition

To address the complex residual noise of "triangle-zone surface wave scattering" that persists after conventional suppression methods, this study introduces an intelligent model-

ing and suppression approach based on matrix singular value decomposition (SVD) [21–23]. Due to the strong scattering and highly non-stationary characteristics of triangle-zone surface waves in the time-space-frequency domain, conventional filtering struggles to protect primary reflections while suppressing noise. By constructing seismic data matrices within localized time windows and frequency bands, this method performs SVD and utilizes adaptive feature selection criteria (e.g., energy ratio and spatial coherence) to dynamically identify and extract eigen-images associated with the scattered surface-wave noise. Consequently, a four-dimensional noise model varying with frequency, time, space, and local signal-to-noise ratio (SNR) is constructed [24]. Subsequent adaptive noise subtraction achieves high-fidelity suppression within zones of strong scattered noise, significantly improving the continuity of reflection events and the overall SNR of seismic sections. This provides a cleaner data foundation for subsequent pre-stack inversion and attribute interpretation, which is illustrated in Figure 5.

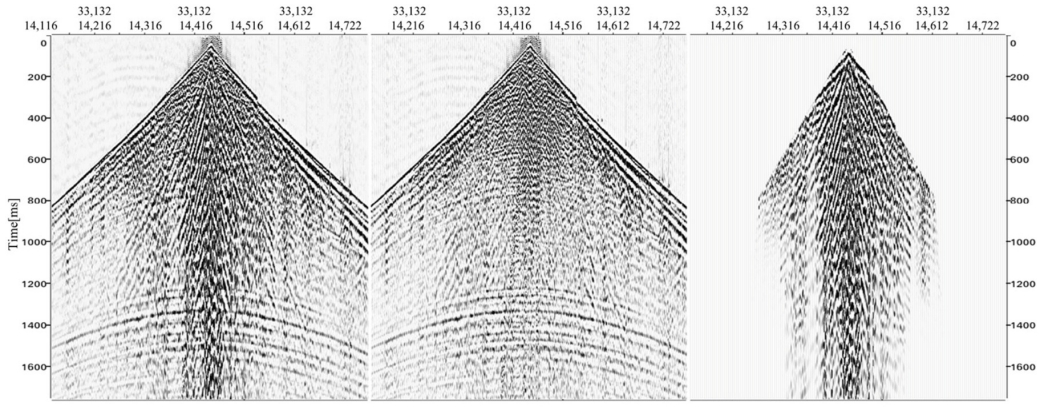


Figure 5. Comparison of seismic data before (**a**) and after (**b**) MSVD-based fidelity-preserving noise attenuation, and the removed noise (**c**).

3.2. Robust Deconvolution Constrained by a Desired Wavelet

To address the lateral non-consistency of signals caused by complex surface conditions and source-receiver disparities, this processing elevates surface-consistent deconvolution from traditional statistical approaches to a deterministic inversion method. Traditional statistical deconvolution typically estimates an average deconvolution operator based on the overall characteristics of the data within a fixed time window. When the signal-to-noise ratio (SNR) is low or lateral variations are strong, traditional statistical deconvolution is highly susceptible to noise and localized heterogeneity, thereby weakening the amplitude characteristics of primary reflections and distorting phase relationships [25–27]. In contrast, the deterministic inversion method employed in this study is based on near-surface models and wavefield propagation constraints. By integrating high-precision first-break picks with the near-surface velocity structure, it inverts spatially adaptive deconvolution operators (Equation (1)), thereby achieving more targeted corrections for surface effects and wavelet variations while effectively suppressing surface-related wavelet interference. This method significantly enhances robustness against random noise and localized anomalies while better preserving the relative amplitude relationships and waveform fidelity of deep weak reflections.

The processing results demonstrate that the lateral consistency of the seismic data is markedly improved, with enhanced continuity of reflection events and clearer responses from thin layers and weak reflections. Figure 6 demonstrates how this establishes a more

consistent and reliable signal foundation for subsequent high-resolution imaging, pre-stack attribute analysis, and fine-grained reservoir prediction.

$$spetrum(trace) = G + s(src) + h(\mathrm{det}) + e(cmp) + q(offset) \quad (1)$$

where $spetrum(trace)$ represents the spectrum of a single-trace seismic record; G denotes the global baseline component of the spectrum, reflecting the average background characteristics of the data; $s(src)$ denotes the receiver term, which reflects the modulation of seismic records by variations in receiver locations and near-surface conditions; $e(cmp)$ signifies the common midpoint (CMP) term, embodying lateral variations related to the midpoint location; and $q(offset)$ represents the offset term, which is used to describe the differences in spectral responses under varying source-receiver offsets.

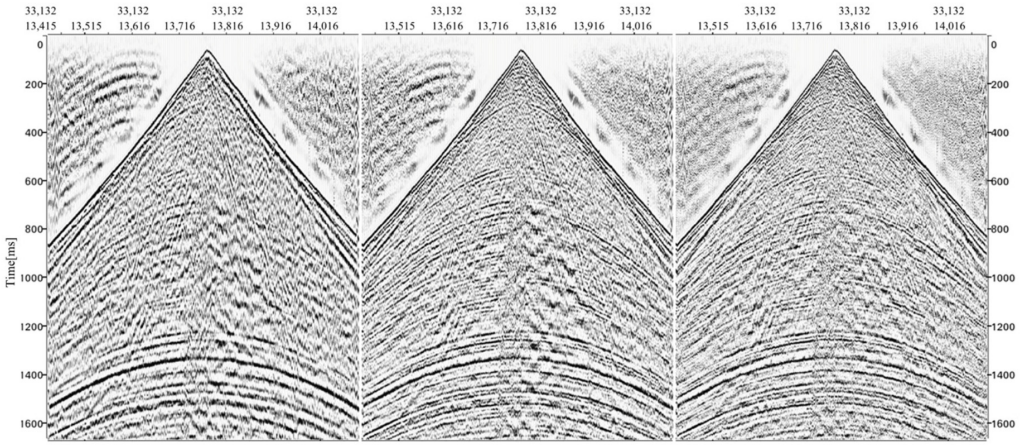


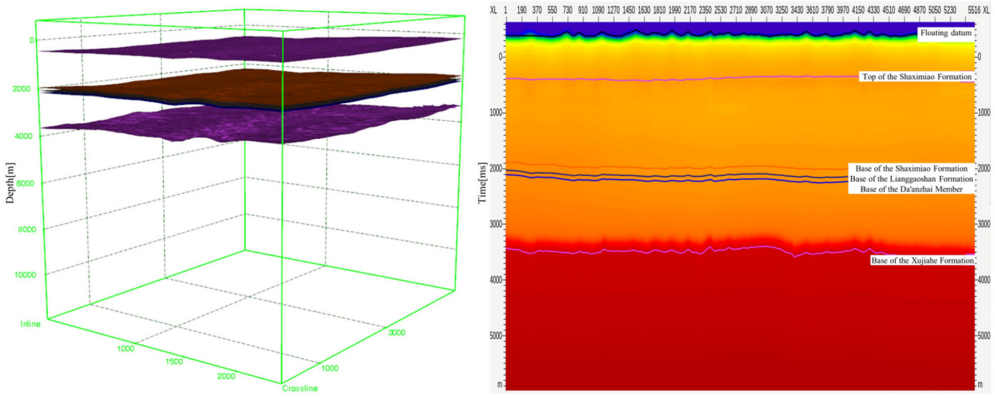
Figure 6. Comparison of seismic data before (**a**) and after (**b**) desired-wavelet-constrained robust deconvolution, and comparison with predictive deconvolution results (**c**).

3.3. "True-Surface" Anisotropic Depth-Domain Velocity Modeling and Imaging

3.3.1. Well-Constrained TTI Initial Velocity Field Building

Building upon the integration of a high-precision near-surface model, an initial velocity field was constructed under the constraint of well logging data. Subsequently, the velocity model was optimized using data-driven full-azimuth angle-domain tomography, enabling "true-surface" TTI anisotropic pre-stack depth migration (PSDM) [28–30].

Analysis of well logs across the survey area indicates that vertical velocity trends are broadly consistent across different locations. The primary velocity contrast interfaces correspond to the base of the Shaximiao Formation, the base of the Lianggaoshan Formation, the base of the Da'anzhai Member, and the base of the Xujiahe Formation. In the time domain, acoustic impedance interfaces with high signal-to-noise ratios (SNRs) were selected for horizon interpretation at a 10 × 10 grid density, including the Suining Formation, the base of the Shaximiao Formation, the base of the Lianggaoshan Formation, the base of the Da'anzhai Member, and the base of the Xujiahe Formation. By integrating well velocity logs with the 3D horizon model, the initial velocity model was established, as shown in Figure 7.



(**a**) (**b**)

Figure 7. Map views (**a**) and vertical profiles (**b**) of the well-constrained TTI initial velocity model.

3.3.2. Full-Azimuth Angle-Domain Grid Tomography Iteration

In this study, the velocity modeling employed full-azimuth grid tomography. By comprehensively leveraging diverse traveltime information—including first arrivals, reflected waves, and diffracted waves—the constraint capabilities and information utilization efficiency of velocity inversion are significantly enhanced. Compared with conventional tomographic methods, this technique is no longer restricted to single-wavefield or localized traveltime constraints. Instead, it performs joint inversion of the subsurface velocity field across multi-azimuth and multi-scale perspectives. Consequently, it enables a finer characterization of complex velocity layers with strong lateral variations and pronounced vertical heterogeneity, such as volcanic bodies, salt domes, and fault damage zones [31,32]. By incorporating denser grid control, the velocity model can better describe local lateral and vertical velocity variations in complex structural zones. In addition, stronger wavefield constraints introduce more reliable information from the observed seismic response, which improves the consistency between the inverted velocity field and the actual wave propagation characteristics. As a result, the velocity–depth relationship can be characterized more accurately, thereby reducing the non-uniqueness and uncertainty of imaging underlying strata. Following full-azimuth grid tomography optimization, the degree of match between the velocity model and the actual wavefield response is further increased. Diffracted waves are more thoroughly focused and collapsed, fault boundaries and structural inflection zones are imaged with superior clarity, and interbedding contact relationships as well as structural details are identified more definitively.

Meanwhile, the velocity model exhibits heightened sensitivity to localized anomalies, which helps mitigate stretching, misalignments, and blurring effects in migration imaging, thereby improving the overall resolution, continuity, and reliability of the seismic sections. This velocity model provides a more robust foundation for complex structural hydrocarbon accumulation analysis, fault system identification, and detailed reservoir prediction, while laying a solid cornerstone for subsequent high-precision imaging and geological interpretation.

4. Results

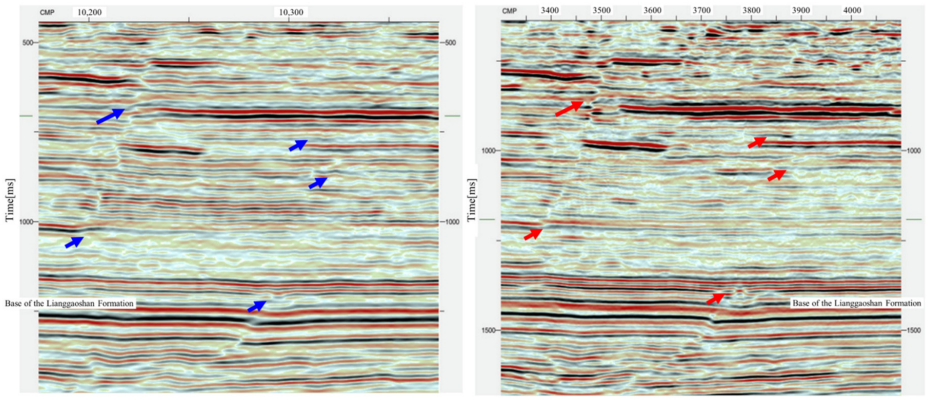
A comprehensive evaluation based on the phased processing results of the high-density seismic data demonstrates that, compared with conventional 3D seismic data, the high-density data exhibits distinct advantages in frequency bandwidth, imaging quality of geological bodies and fault systems, and overall seismic resolution. Specifically, the delineation precision of channel planforms has been refined from ~180 m to ~60 m, and small-scale faults with vertical throws as small as ~5 m are effectively resolved. This

significantly enhances the identification of thin-bedded sandbodies and subtle structures, providing a more reliable data foundation for the fine-grained evaluation of shale oil reservoir sweet spots.

Before comparing the imaging results of the 2019 and 2025 datasets, it should be noted that the comparison involves both acquisition and processing differences. Therefore, the improvement observed in the 2025 dataset should not be attributed solely to processing enhancement. Instead, it reflects the combined contribution of optimized high-density acquisition and the corresponding high-fidelity processing workflow. The optimized acquisition design provided broader bandwidth, higher fold coverage, and better prestack amplitude preservation, whereas the processing workflow further improved the signal-to-noise ratio, wavelet consistency, resolution, velocity accuracy, and imaging quality. The evaluation was conducted across the following four aspects.

4.1. Overall Evaluation of Seismic Data

Based on the evaluation of the processing results, the high-density 3D seismic data in the Gongshanmiao area exhibits distinct advantages over conventional 3D seismic data in terms of bandwidth, imaging of geological bodies and faults, and resolution. The frequency band of the data has been extended from 6–78 Hz to 4–90 Hz, and the dominant frequency has increased from 35 Hz to 42 Hz. The overall signal-to-noise ratio (SNR) is high, characterized by clearly discernible reflection wave groups, dynamic waveform responses, accurate migration positioning, and favorable lateral continuity of reflection events. Furthermore, fault terminations are sharp, channel reflection characteristics are prominent, and channel "bright spots" are more intuitively identifiable. As illustrated in Figure 8, this establishes a high-quality data foundation for subsequent structural interpretation and fine-grained reservoir evaluation.



(**a**) (**b**)

Figure 8. Comparison of fault characterization between the 2019 Xichong (**a**) and current 3D (**b**) prestack time migration profiles.

4.2. Fault Imaging Evaluation

The comprehensive comparative results demonstrate that faults with vertical throws exceeding 15 m are clearly resolved in both high-density and conventional 3D seismic data, exhibiting sharp fault terminations and prominent offset features, yielding comparable identification performance. For minor faults with vertical throws of 10–15 m, both datasets capture favorable seismic responses; however, the high-density data provides superior delineation of their planform geometries and spatial continuity, thereby facilitating the verification of subtle structural details.

For small-scale faults with vertical throws of 6–10 m, the advantages of high-density data in terms of signal-to-noise ratio (SNR) and resolution become markedly more pro-

nounced. On seismic sections, these faults predominantly manifest as distinct flexing or subtle offsetting of reflection events, rendering their seismic signatures much easier to recognize. Meanwhile, the high-density data exhibits superior imaging capabilities in complex structural zones, delineating fault characteristics more clearly, producing sharper fault-plane reflections, and clarifying the contact relationships between channel boundaries and minor faults. Consequently, this enhances the overall reliability of structural framework interpretation, as shown in Figure 9.

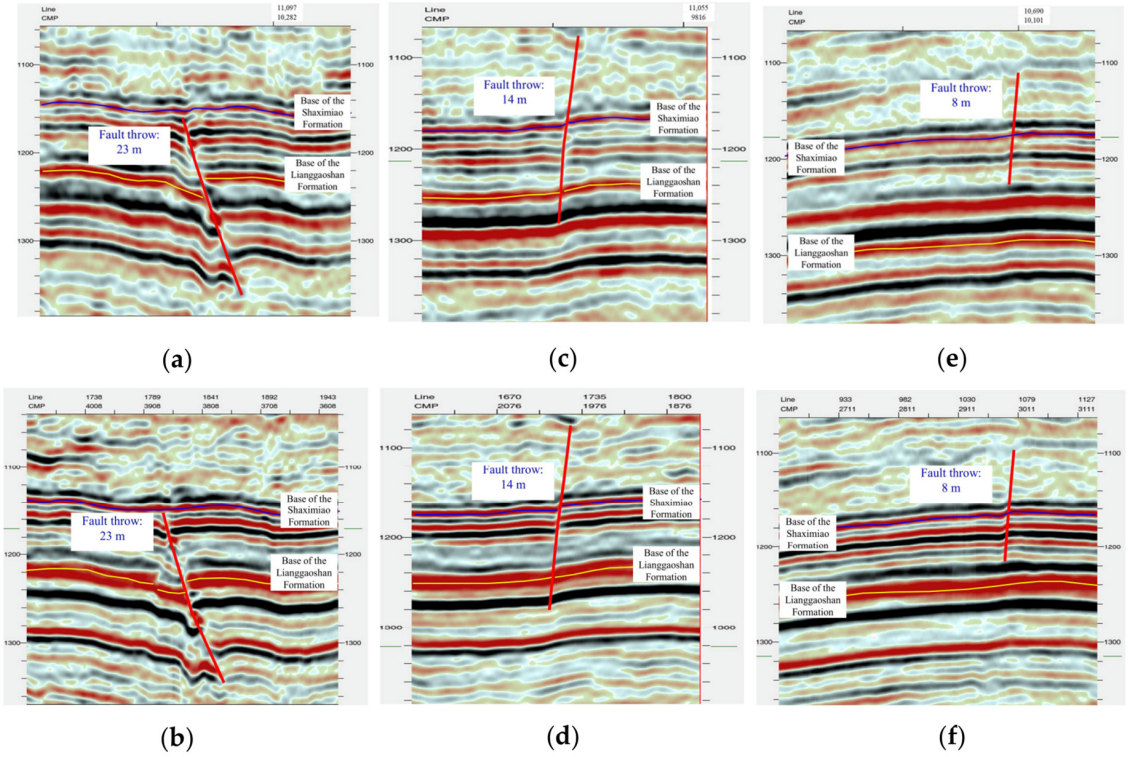
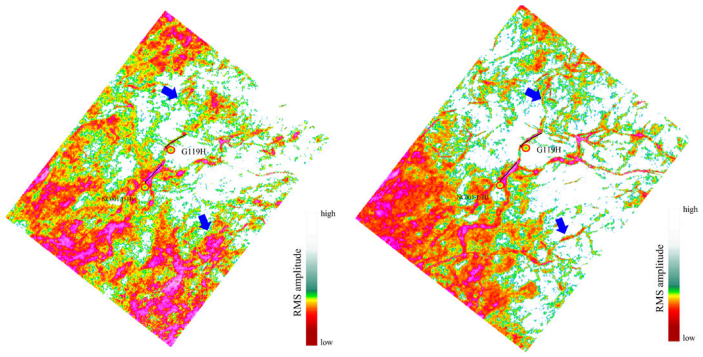


Figure 9. Comparison of fault imaging evaluation at different displacements between the 2019 Xichong (**a**,**c**,**e**) and current 3D (**b**,**d**,**f**) prestack time migration profiles.

4.3. Channel Sandbody Identification Evaluation

Compared with conventional data, the newly processed data exhibit clearer channel reflection characteristics, superior wave group continuity, and more stable internal "bright spots" and boundary responses within the target interval. This significantly enhances the identification capability and resolving power for narrow channels and thin sandbodies. Particularly in the oil-bearing Liang-2 Member (the second member of the Lianggaoshan Formation) in the Gongshanmiao area, the new data further refine the delineation precision of channel sandbodies, yielding more complete channel morphologies and stronger planform continuity. Figure 10 demonstrates how the imaging effect of narrow channels has been remarkably improved, with the channel planform delineation resolution sharpening from the original ~180 m to ~60 m. Overall, the new dataset not only improves the resolvability and trackability of the target sandbodies but also provides a more reliable seismic foundation for analyzing channel sandbody distribution patterns and conducting subsequent fine-grained reservoir evaluations.

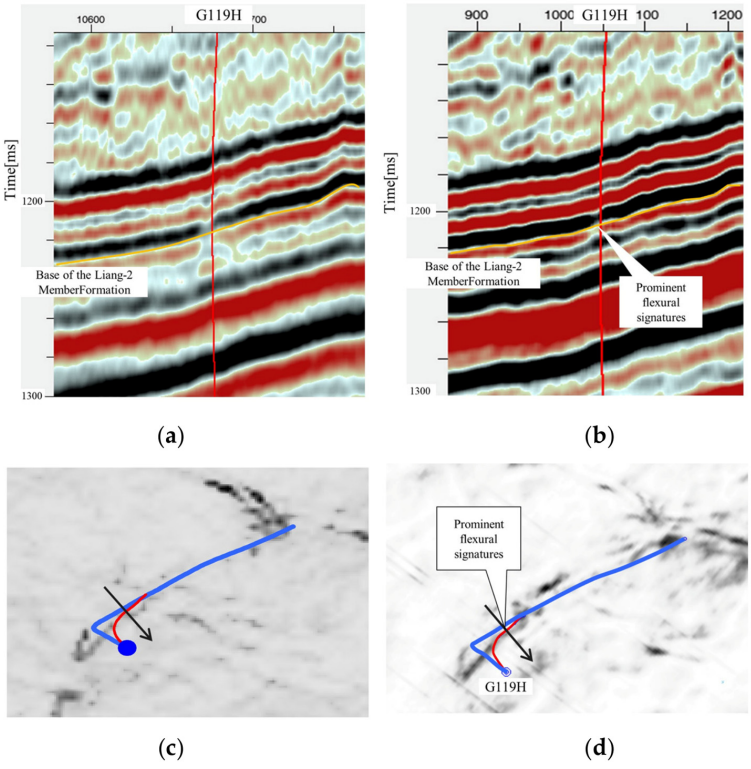


(**a**) (**b**)

Figure 10. Comparison of RMS attribute maps of the Liang-2 Member between the 2019 Xichong (**a**) and current 3D (**b**) prestack time migration results.

4.4. Validation by Drilling Results

Taking the representative well Gong-119 as an example, the actual drilling results provide robust validation for the aforementioned seismic interpretation. Coring at the base of the Liang-2 Member in this well revealed a sandstone with a true vertical thickness (TVT) of approximately 5 m, corresponding to a measured thickness of about 6.6 m along the borehole. This indicates the development of a sandstone reservoir with a verifiable thickness within the target interval. Core observations indicate that fractures are highly developed throughout the sandstone interval, featuring multiple low-angle fractures, which suggests favorable fracture stimulation potential and enhanced permeability connectivity for fluid flow pathways. Concurrently, the cored sandstone interval exhibits excellent oil-bearing properties, consisting of 3.6 m (TVT) of oil-saturated sandstone and 1.4 m (TVT) of oil-stained sandstone. This reflects favorable hydrocarbon charging conditions and distinct reservoir sweet spot characteristics, as shown in Figure 11.



(**a**) (**b**)

(**c**) (**d**)

Figure 11. Comparison of seismic profiles crossing Well Gong-119 and symmetry attribute maps between the 2019 Xichong (**a**,**c**) and current 3D (**b**,**d**) prestack time migration.

The close agreement between the actual coring results and the seismic interpretations demonstrates the high reliability of the new dataset in predicting sandbody distribution, thickness variations, and favorable reservoir fairways within the Liang-2 Member. It further validates the efficacy of high-density seismic data for narrow channel identification, thin sandbody characterization, and sweet spot evaluation, thereby providing strong support for subsequent well targeting and detailed reservoir evaluation in the study area.

5. Discussion

The seismic data processing workflow in this study was designed with the core objectives of achieving high fidelity, high resolution, and high-precision imaging. To address the key challenges of seismic data processing under complex geological conditions, an integrated processing framework was established, which included noise suppression, resolution enhancement, velocity modeling, and fine imaging. This workflow effectively improves the quality of seismic data and provides reliable support for fine geological and reservoir characterization. The workflow can be divided into three main technical modules: high-fidelity noise suppression, well-constrained high-resolution processing, and integrated full-sequence velocity characterization and fine imaging. These modules differ in their technical principles, applicable conditions, and limitations.

High-fidelity noise suppression is a key step in the seismic data preprocessing stage. In this study, it mainly includes matrix singular value decomposition-based suppression of black-triangle coherent noise and stationary wavelet transform-based suppression of abnormal-amplitude noise. The main objective of this module is to remove different types of noise while preserving the amplitude, phase, and waveform characteristics of effective subsurface reflections as much as possible. This step improves the signal-to-noise ratio of seismic data acquired under complex surface and acquisition conditions, and provides a reliable data basis for subsequent high-resolution processing and high-precision migration imaging. This module is particularly suitable for complex surface areas, such as mountainous regions, gobi areas, and loess tablelands, where excitation and receiving conditions are poor and various types of coherent noise, random noise, and abnormal-amplitude interference are commonly observed. However, this technique also has some limitations. When the spectral or coherent characteristics of noise strongly overlap with those of effective reflections, complete separation is difficult and residual noise may remain. In highly fractured zones, weak geological signals may also be mistakenly suppressed as noise [33,34]. In addition, the processing result is sensitive to parameter selection, and inappropriate parameters may cause waveform distortion or amplitude loss.

Well-constrained high-resolution processing is the key step for improving the vertical resolution of seismic data. In this study, robust deconvolution constrained by an expected wavelet was used. With the constraint of measured well data, such as sonic logs, this method corrects the seismic wavelet and broadens the effective frequency bandwidth of the seismic data. It reduces the non-uniqueness of conventional deconvolution and improves the vertical identification accuracy of thin layers. This module is suitable for areas with sufficient borehole and logging data, especially for thin reservoirs and thin interbedded strata. It contributes directly to fine stratigraphic correlation, thin-bed reservoir prediction, and the preparation of high-fidelity and high-resolution gathers for subsequent velocity modeling and migration imaging. Nevertheless, its effectiveness depends strongly on the quality of well data. In areas with few wells or poor well-log quality, the advantage of this method may be limited. If obvious time-depth mismatch or phase inconsistency exists between well and seismic data, errors may be introduced into wavelet estimation. Moreover, due to the physical limitation of wave propagation and noise conditions, the frequency bandwidth of deep weak-energy signals cannot be broadened indefinitely. For

low signal-to-noise-ratio data, robust deconvolution may also generate false thin-bed responses and thus affect geological interpretation.

The integrated full-sequence velocity characterization and fine imaging module includes micro-logging-constrained tomographic near-surface modeling, angle-domain full-azimuth grid tomography, and true-surface TTI anisotropic prestack depth migration. Through high-precision near-surface and subsurface velocity modeling, anisotropic correction, absorption compensation, and accurate migration imaging, this module improves the spatial positioning of subsurface geological bodies and reduces imaging distortion, structural mispositioning, and blurred fault images in complex surface and structural areas. It is especially applicable to areas with strong surface relief, rapid lateral velocity variation in the near surface, severe static correction problems, and complex subsurface structures such as faults, folds, and thrust belts. This module supports full-sequence structural interpretation, fault-system characterization, complex reservoir imaging, and fine reservoir modeling. However, the imaging accuracy depends highly on the density and reliability of well-control and near-surface constraint data. Sparse or unrepresentative constraint data may reduce the accuracy of the velocity model and further affect imaging quality. In addition, TTI anisotropic modeling involves multiple parameters and strong non-uniqueness. Improper parameter estimation may lead to imaging distortion or structural positioning errors. The workflow is also computationally intensive and requires high hardware resources and processing costs. In extremely fractured or strongly scattering formations, imaging ambiguity and local detail loss may still occur even when high-precision migration imaging is applied. Errors generated during near-surface modeling may also propagate downward and influence the imaging quality of middle and deep formations.

6. Conclusions

(1) Based on a comprehensive review of previous workflows and the specific seismic data characteristics of the study area, processing parameters were systematically optimized. High-fidelity pre-stack noise attenuation effectively suppressed noise while preserving weak signals associated with subtle structures and small-scale faults, thereby enhancing data fidelity. High-resolution, well-constrained consistent processing was implemented to fully exploit data potential, improving both vertical resolution and thin-reservoir resolving capability. Combined with high-precision velocity modeling, migration positioning accuracy for subtle structures and faults was significantly improved, clarifying the lateral distribution of reservoirs. Consequently, the final results achieved a high signal-to-noise ratio (SNR), high resolution, and high fidelity, providing a solid data foundation for subsequent geological interpretation.

(2) Compared with conventional 3D seismic data, the high-density dataset exhibits clear advantages in fault identification, thin-bed resolution, and channel delineation. In particular, the planar characterization accuracy of channels was improved from approximately 180 m to 60 m, corresponding to a reduction in uncertainty of about 66.7% and a threefold improvement in channel delineation precision. The high-density dataset also yields sharper imaging of minor faults and narrow channels. Validation with drilling results from Well Gong-119 further demonstrates that the optimized processing workflow is reliable for thin-sandbody prediction, fault identification, and sweet spot evaluation.

(3) This study delivers a dependable framework for structural interpretation, reservoir evaluation, and well targeting within the Lianggaoshan Formation and associated intervals in the Gongshanmiao block. Furthermore, the technical achievements and methodology presented here hold substantial value for replication and reference in

other exploration areas characterized by complex structures, thin interbedded strata, and narrow channel networks.

(4) Although full-coverage high-density 3D seismic acquisition can significantly improve imaging accuracy and the characterization of complex structures and thin reservoirs, its large field workload, high equipment investment, long acquisition period, and high exploration cost limit its large-scale application. Future research should therefore focus on the degradation and fusion of high-density 3D seismic data. A hierarchical and complementary fusion strategy is recommended, in which newly acquired shallow high-resolution and high-density data are used to improve the imaging of shallow structures, faults, and reservoir details, while historical deep seismic data are fully utilized for deeper targets. This approach can retain the high-resolution and high-accuracy imaging advantages of high-density seismic data while reducing repeated acquisition, field workload, exploration cost, and acquisition time, thereby providing a more efficient and scalable approach for high-precision seismic exploration.

Author Contributions: Conceptualization, M.Z. and B.H.; methodology, Q.T. and D.Z.; software, Z.L. and X.Y.; validation, F.L.; formal analysis, H.P.; investigation, X.Y. and C.T.; resources, D.Z.; data curation, D.Z.; writing—original draft preparation, M.Z. and D.Z.; writing—review and editing, B.H. and Z.L.; visualization, F.L. and Z.T.; supervision, H.P.; project administration, X.Y.; funding acquisition, M.Z. All authors have read and agreed to the published version of the manuscript.

Funding: This research was funded by the Exploration and Development Research Institute of the PetroChina Southwest Oil and Gas Field Company through project DFWT-XNWTTFGS-2025-JS-751, titled "2025 3D Seismic Exploration Project of Crude Oil in Gongshanmiao Block, Shunqing Oilfield, Sichuan Basin".

Data Availability Statement: The original contributions presented in this study are included in the article. Further inquiries can be directed to the corresponding author.

Conflicts of Interest: Authors Ming Zeng and Zhihui Tu were employed by the Exploration and Development Research Institute of the PetroChina Southwest Oil and Gas Field Company. Authors Bing He, Fei Li and Haotian Peng were employed by the Development Management Department, PetroChina Southwest Oil and Gas Field Company. Authors Qingsong Tang and Cong Tang were employed by the Crude Oil Department, PetroChina Southwest Oil and Gas Field Company. Authors Zhigang Liu and Xiaowei Yan were employed by the Southwest Geophysical Research Institute, BGP Inc., China National Petroleum Corporation. The remaining authors declare that they have no commercial or financial relationships that could be construed as a potential conflict of interest. This study received funding from the Exploration and Development Research Institute of the PetroChina Southwest Oil and Gas Field Company. The funder was not involved in the study design; collection, analysis, or interpretation of data; the writing of this article; or the decision to submit it for publication.

References

1. Yang, Y.; Yang, J.; Yang, G.; Tao, S.; Ni, C.; Zhang, B.; He, X.; Lin, J.; Huang, D.; Liu, M.; et al. New Research Progress of Jurassic Tight Oil in Central Sichuan Basin, SW China. *Pet. Explor. Dev.* **2016**, *43*, 954–964. [CrossRef]
2. Yang, G.; Huang, D.; Huang, P.; Yan, W.; Yang, T.; Dai, H.; Lin, J. Control Factors of High and Stable Production of Jurassic Da'anzhai Member Tight Oil in Central Sichuan Basin, SW China. *Pet. Explor. Dev.* **2017**, *44*, 866–875. [CrossRef]
3. Chen, S.; Gao, X.; Wang, L.; Lu, J.; Liu, C.; Tang, H.; Zhang, H.; Huang, Y.; Ni, S. Factors Controlling Oiliness of Jurassic Lianggaoshan Tight Sands in Central Sichuan Basin, SW China. *Pet. Explor. Dev.* **2014**, *41*, 468–474. [CrossRef]
4. Jiang, Q.; Lu, J.; Xiao, Z.; Qin, C.; Liu, Z.; Li, Y.; Zhu, X.; Zhou, X. Hydrocarbon Generation Mechanism of Shallow Lacustrine Basin Shales Rich in Exinite in Early Jurassic. *J. Asian Earth Sci.* **2025**, *294*, 106768. [CrossRef]
5. Li, D.; Li, J.; Zhang, B.; Yang, J.; Wang, S. Formation Characteristics and Resource Potential of Jurassic Tight Oil in Sichuan Basin. *Pet. Res.* **2017**, *2*, 301–314. [CrossRef]
6. Pang, Z.; Tao, S.; Zhang, Q.; Zhang, T.; Yang, J.; Fan, J.; Yuan, M. Enrichment Factors and Sweep Spot Evaluation of Jurassic Tight Oil in Central Sichuan Basin, SW China. *Pet. Res.* **2019**, *4*, 334–347. [CrossRef]

7. Chen, S.; Zhang, H.; Lu, J.; Yang, Y.; Liu, C.; Wang, L.; Zou, X.; Yang, J.; Tang, H.; Yao, Y.; et al. Controlling Factors of Jurassic Da'anzhai Member Tight Oil Accumulation and High Production in Central Sichuan Basin, SW China. *Pet. Explor. Dev.* **2015**, *42*, 206–214. [CrossRef]
8. Su, N.; Chen, Z.; Yang, W.; Wang, L.; Li, W.; Yang, C.; Li, R.; Zhang, L.; Ma, X.; Zhang, H. Features and Favorable Exploration Direction of Normal Faults in Jurassic Strata in Northern Central Sichuan Basin, China. *J. Nat. Gas. Geosci.* **2023**, *8*, 413–426. [CrossRef]
9. Zhang, B.-Y.; Peng, J.-M.; Ge, D. A Fluidic Hammer as a High-Fidelity Seismic-While-Drilling Source: A Direct, Quantitative Comparison with Conventional Drill Bits. *Pet. Sci.* **2026**, S1995822626003717. [CrossRef]
10. Yang, H.; Cheng, Y.; Li, G. A Denoising Method for Ship Radiated Noise Based on Spearman Variational Mode Decomposition, Spatial-Dependence Recurrence Sample Entropy, Improved Wavelet Threshold Denoising, and Savitzky-Golay Filter. *Alex. Eng. J.* **2021**, *60*, 3379–3400. [CrossRef]
11. Cai, K.; Ma, J. Ground Rolls Attenuation via Gradient Flow Regularization. *J. Appl. Geophys.* **2018**, *155*, 246–255. [CrossRef]
12. Yan, T.; Dai, Y.; Wang, Z. Ground-Roll Attenuation in High-Dimensional Domain Using Multi-Scale Decomposition and Attention Mechanism Network. *J. Appl. Geophys.* **2025**, *239*, 105736. [CrossRef]
13. Guo, M.; Wu, Z. Noise Reduction for High-Accuracy Automatic Calibration of Resolver Signals via DWT-SVD Based Filter. *Electronics* **2019**, *8*, 516. [CrossRef]
14. Lu, J.; Wang, Y.; Chen, J. Noise Attenuation Based on Wave Vector Characteristics. *Appl. Sci.* **2018**, *8*, 672. [CrossRef]
15. Wang, W.; Gao, J.; Chen, W.; Xu, J. Data Adaptive Ground-Roll Attenuation via Sparsity Promotion. *J. Appl. Geophys.* **2012**, *83*, 19–28. [CrossRef]
16. Gao, K.; Huang, L.; Cladouhos, T. Seismic Characterization of the Blue Mountain Geothermal Field. *Energies* **2023**, *16*, 5822. [CrossRef]
17. Xiao, L.; Zhang, Z.; Gao, J. Ground Roll Attenuation of Multicomponent Seismic Data with the Noise-Assisted Multivariate Empirical Mode Decomposition (NA-MEMD) Method. *Appl. Sci.* **2022**, *12*, 2429. [CrossRef]
18. Xue, Y.; Cao, J.; Tian, R.; Du, H.; Shu, Y. Application of the Empirical Mode Decomposition and Wavelet Transform to Seismic Reflection Frequency Attenuation Analysis. *J. Pet. Sci. Eng.* **2014**, *122*, 360–370. [CrossRef]
19. Cheng, Q.; Cui, F.; Chen, B.; Dong, G.; Wang, R.; Zhang, G.; Fu, J. Attenuation of Non-Stationary Random Noise in Ground Penetrating Radar Data Based on Time-Varying Filtering. *Measurement* **2024**, *236*, 115169. [CrossRef]
20. Mei, J.; Xue, Y.; Duan, Y. Strong Amplitude Suppression of Seismic Data Using Maximum Energy Method Based on MVMD. *J. Appl. Geophys.* **2026**, *249*, 106186. [CrossRef]
21. Lv, H. Single-Channel and Multi-Channel Seismic Random Noise Suppression Based on the Regularized Non-Stationary Decomposition. *J. Appl. Geophys.* **2020**, *175*, 103986. [CrossRef]
22. Huang, W.-L.; Zhou, Y.-X.; Zhou, Y.; Liu, W.-J.; Li, J.-D. A Reweighted Damped Singular Spectrum Analysis Method for Robust Seismic Noise Suppression. *Pet. Sci.* **2024**, *21*, 1671–1682. [CrossRef]
23. Shioi, A.; Otake, Y. A Fundamental Study on Introducing Time-Delay Embedding to Enhance the Applicability of Dynamic Mode Decomposition for Seismic Response Analysis. *Soil Dyn. Earthq. Eng.* **2026**, *200*, 109806. [CrossRef]
24. Zhang, D.; Rui, Z.; Ma, Y.; Wang, R. Robust Damped Multichannel Singular Spectrum Analysis with Adaptive Correction: A Parameter-Tolerant Approach for Seismic Data Denoising and Separation. *J. Appl. Geophys.* **2026**, *251*, 106260. [CrossRef]
25. Du, Z.; Liu, D.; Jiang, Z.; Zha, C.; Cui, L. Network-Optimized Sparse Deconvolution with Statistical-Temporal Constraints: A Robust Blind Framework for Repetitive Fault Extraction in Rolling Bearings. *Mech. Syst. Signal Process.* **2025**, *238*, 113183. [CrossRef]
26. Han, S.; Moon, S.; Jun, H.; Kim, Y.; Shen, Y.; Cho, Y. A Stochastic Deconvolution via Trans-Dimensional Markov-Chain Monte Carlo. *J. Appl. Geophys.* **2026**, *245*, 106063. [CrossRef]
27. Shi, G.; Gu, X.; Liu, Y.; Zhang, Z.; Yang, S. ENAS–SCMNet: A Novel Efficient Neural Architecture Search–Driven Blind Deconvolution Network Based on Statistical Complexity Measure for Railway Bearing Fault Diagnosis. *Eng. Fail. Anal.* **2026**, *185*, 110401. [CrossRef]
28. Zhao, H.; Wang, X.; Cai, Y.; Liu, W. Wetland Transitions and Protection under Rapid Urban Expansion: A Case Study of Pearl River Estuary, China. *Sustainability* **2016**, *8*, 471. [CrossRef]
29. Behera, L. Elastic Anisotropic Finite-Difference Full-Wave Modeling and Imaging of 2D Tilted Transversely Isotropic (TTI) Media. *J. Appl. Geophys.* **2022**, *207*, 104837. [CrossRef]
30. Maćkowski, T.; Zając, A.; Hadro, P.; Cygal, A.; Stefaniuk, M. Cutting-Edge Reverse Time Migration Imaging of the Hydrocarbon Deposits in the Outer Carpathian Fold-Thrust Belt. *Mar. Pet. Geol.* **2025**, *181*, 107515. [CrossRef]
31. Zhuang, S.-B.; Huang, J.-P.; Yang, J.-D.; Li, Z.-C. A Computational Method for Wide-Azimuth 3D Dip-Angle Gathers Using Gaussian Beam Migration. *Pet. Sci.* **2022**, *19*, 2081–2094. [CrossRef]
32. Rasgado-Moreno, C.-O.; Rist, M.; Land, R.; Ratassepp, M. Guided Wave Tomography of Pipe Bends Based on Full Waveform Inversion. *Ultrasonics* **2025**, *148*, 107560. [CrossRef]

33. Li, Y.; Yang, J.; Yu, Q.; Liu, X.; Guo, W.; Miao, S. 3D Coupled Dynamic Modeling of Deep Shaft Excavation near a Fault: Coseismic Slip and Seismic Hazards. *J. Rock Mech. Geotech. Eng.* **2025**. [CrossRef]
34. Li, Y. Spatial Distribution of Strain Energy Changes Due to Mining-Induced Fault Coseismic Slip: Insights from a Rockburst at the Yuejin Coal Mine, China. *Rock Mech. Rock Eng.* **2025**, *58*, 1693–1706. [CrossRef]

Disclaimer/Publisher's Note: The statements, opinions and data contained in all publications are solely those of the individual author(s) and contributor(s) and not of MDPI and/or the editor(s). MDPI and/or the editor(s) disclaim responsibility for any injury to people or property resulting from any ideas, methods, instructions or products referred to in the content.